CHAPTER 1

INTRODUCTION

Zinc oxide (ZnO) is an n-type semiconductor with many attractive features. The assorted physical properties such as electro-optical, acusto-optical, piezoelectrical, and luminescence characteristics, render the thin film of ZnO a liable material for a variety of applications. ZnO with the wide band gap of 3.37 eV at low temperature and 3.20 eV at room temperature is transparent to most of the solar spectrum. ZnO thin films have attracted interest as a low-cost alternative to indium tin oxide (ITO), light modulators, optical sensors, gas sensors, photocatalysts polymer-based solar cells, optical wave guides and etc. [1].

Polymer-based solar cells have received increasing attention for the advantages such as low-cost, light weight and large size. However, compared with traditional inorganic photovoltaics, the polymer-based devices are still limited in their performance because of the drawbacks such as the weak absorption in the visible long-wavelength, poor charge transport, and low stability. Recently, methods to further improve performance of the polymer based solar cells have been actively explored through the optimization of materials and device structures. By implementing a bulk-heterojunction of p- and n-type semiconductor, the efficiency of such solar cells has been greatly increased. The devices have been prepared by blending a p-type semiconductor polymer with microseparated n-type semiconductors (e.g., n-type polymer, TiO_2, ZnO, CdSe, and C_{60} derivatives) [2].

ZnO nanostructure gas sensors have been widely investigated and are reported to show increases of sensitivity and the reductions of response time. In addition, metal doping such as Au, Pt or Pd, etc. in oxide semiconductors is a typical method used to enhance sensing properties. The metal dopant acts as a catalyst to modify surface reactions of metal oxide semiconductors toward sensing gases. Several studies have been reported on the enhancement of sensitivity and stability of sensors using doping with metal catalysts [3].

Photocatalytic degradation of organic pollutants in water and air using semiconductive particles, such as TiO_2 and ZnO, has attracted extensive attention in the past two decades [4]. In particular, ZnO has attracted much attention with respect to the degradation of various pollutants due to its high photosensitivity, stability and wide band gap. While TiO_2 is widely employed as a photocatalyst, ZnO is a suitable alternative to TiO_2 as it has a similar band gap energy (3.2 eV) [5], larger quantum efficiency than TiO_2 and higher photocatalytic efficiencies were reported [6].

Typically, for their application nanostructures based on ZnO can be fabricated by various growth techniques. One interesting technique is a FSP technique which is simple with low cost [7]. One of the advantages of this technique is that even materials containing several constituents such as mixed oxides or supported metal particles can be prepared in one step. Using precursors of high purity, nanomaterials with high chemical grade can be produced. Recently the method has been applied to prepare metal oxide-supported particles and heterogeneous catalysts [8].

In the present study, Niobium doped ZnO (Nb-doped ZnO) nanoparticles were synthesized by FSP and influence of the Nb loading on the zinc oxide support was analyzed in Chapter 2. The polymer solar cells for the enhancement of photoelectric efficiency were fabricated in Chapter 3. The effect of Nb doping concentration on gas

sensing properties of pure ZnO based on results from gas sensing test were discussed in Chapter 4 and the photocatalytic activities of the pure ZnO and Nb-doped ZnO were discussed in Chapter 5.

There are four parts in this chapter consisting of the background of zinc oxide, niobium, flame spray pyrolysis and the theory of characterization techniques.

1.1   Zinc oxide

ZnO generally represented by the formula ZnO. It is amorphous white or yellow in color. But it is commonly present as white powder. ZnO is insoluble in water as only a small amount of this can get dissolved in water to make a solution. The white powder of ZnO occurs as zinc white or as a mineral called zincite and is present in earth's crust. This mineral contains manganese and some other elements. This mineral is yellowish or red in color.

1.1.1 Crystal structure

ZnO exists in three different crystal structures, i.e. hexagonal wurtzite, cubic zincblende, and the rarely observed cubic rocksalt [9]. ZnO is thermodynamically stable in the wurtzite phase due to the effect that the bonding class is exactly at the borderline between covalent and ionic. The lattice constants of wurtzite mostly range from 3.2475 to 3.2501 Å for parameter **a** and from 5.2042 to 5.2075 Å for parameter **c** (see Figure 1.1(a)). The **c/a** ratio varies in a slightly wider range, from 1.593 to 1.6035. The deviation from that of the idea wurtzite crystal is probably due to the lattice stability and electronegativity. A number of studies have been addressed to epitaxial wurtzite ZnO, while a few experimental and theoretical investigations are performed on the metal stable zincblende ZnO growth and its fundamental properties. Zincblende materials have lower ionic character compared to wurtzite materials that has been related to the **c/a** ratio, indicating that zincblende materials are covalent

(Figure 1.1(b)). In the zincblende and wurtzite structures, each Zn (or O) has four nearest neighbors: the in-plane bonds are stronger, as indicated by higher electron density, than the out-of-plane bonds. In contrast to the zincblende/wurtzite structures, in the rocksalt structure each Zn (or O) has six nearest neighbors.
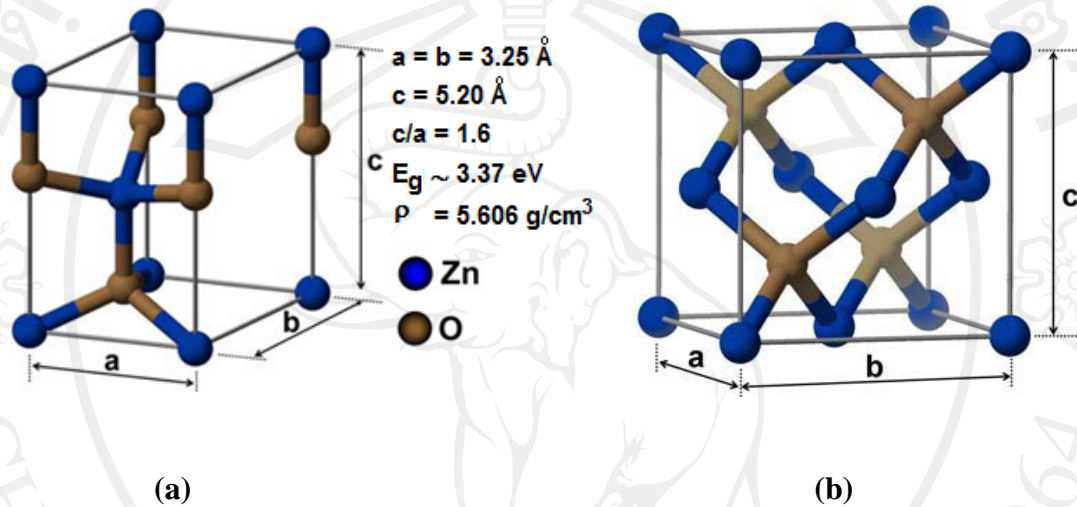

Figure 1.1 Crystal structure of zinc oxide. (a) Wurtzite phase ZnO, (b) Zincblende phase ZnO.

The wurtzite ZnO structure is an ABAB hexagonal close packing structure (space group C6mc) with lattice parameters $a = 0.325$ and $c = 0.520$ nm as illustrated in Figure 1.1(a). The wurtzite-structure ZnO crystal is described as a number of alternating planes composed of tetrahedrally coordinated O^{2-} and Zn^{2+} ions stacked alternately along the c-axis [10]. The oppositely charged ions produce positively charged Zn-(0001) and negatively charged O-($000\bar{1}$)) surfaces, resulting in a normal dipole moment and spontaneous polarization along the c-axis as well as a divergence in surface energy [11]. Besides the {0001} polar surfaces, ZnO has other typical polar surfaces: the $\{10\bar{1}1\}$ surfaces [12]. Interestingly, these polar surfaces make up

hexagonal pyramids. In this model, the hexagonal pyramid consists of an O-terminated $(000\bar{1})$ surface for the base and O-terminated $\{10\bar{1}1\}$ planes for the side surfaces, all of which are polar surfaces. We picture here the O-terminated surfaces because the O-terminated $(000\bar{1})$ polar surface is usually thought to be inert in comparison with the Zn-terminated ZnO (0001) polar surface [10]. The tip of the pyramid is along the [0001] direction, the Zn polarized direction. The calculated angle between two opposite edges at the tip of the pyramid is 63.94º, and the angle between the edge and the base plane is 58.03º.

1.1.2 Mechanical properties

ZnO is a relatively soft material with approximate hardness of 4.5 on the Mohs scale [13]. Its elastic constants are smaller than those of relevant III-V semiconductors, such as GaN. The high heat capacity and heat conductivity, low thermal expansion and high melting temperature of ZnO are beneficial for ceramics [14]. Among the tetrahedrally bonded semiconductors, it has been stated that ZnO has the highest piezoelectric tensor or at least one comparable to that of GaN and AlN [15]. This property makes it a technologically important material for many piezoelectrical applications, which require a large electromechanical coupling.

1.1.3 Electronic properties

ZnO has a relatively large direct band gap of ~3.2 eV at room temperature [16]; therefore, pure ZnO is colorless and transparent. Advantages associated with a large band gap include higher breakdown voltages, ability to sustain large electric fields, lower electronic noise, and high-temperature and high-power operation. The bandgap of ZnO can further be tuned from ~3−4 eV by its alloying with magnesium oxide or cadmium oxide [16].

Most ZnO has n-type character, even in the absence of intentional doping. Nonstoichiometry is typically the origin of n-type character, but the subject remains controversial [17]. An alternative explanation has been proposed, based on theoretical calculations, that unintentional substitutional hydrogen impurities are responsible [18]. Controllable n-type doping is easily achieved by substituting Zn with group-III elements such as Al, Ga, In or by substituting oxygen with group-VII elements chlorine or iodine [19]. Reliable p-type doping of ZnO remains difficult. This problem originates from low solubility of p-type dopants and their compensation by abundant n-type impurities. This problem is observed with GaN and ZnSe. Measurement of p-type in "intrinsically" n-type material is complicated by the inhomogeneity of samples [20]. Current limitations to p-doping do not limit electronic and optoelectronic applications of ZnO, which usually require junctions of n-type and p-type material. Known p-type dopants include group-I elements Li, Na, K; group-V elements N, P and As; as well as copper and silver. However, many of these form deep acceptors and do not produce significant p-type conduction at room temperature [21]. Electron mobility of ZnO strongly varies with temperature and has a maximum of ~2000 cm^2/(V·s) at 80 K [22]. Data on hole mobility are scarce with values in the range 5-30 cm^2/(V·s).

1.1.4 Optical properties

ZnO has a band gap of 3.2 eV, which corresponds to emission in the UV region (300–400 nm). This band gap is very close to that of GaN (3.39eV), and GaN has been the subject of much research over the past years, even being incorporated into the recent Blu-Ray drives. However, ZnO has some significant advantages in its large free exciton binding energy (60 meV compared to 21–25 meV for GaN) that

allows for efficient excitonic emission at room temperature [11]. Table 1.1 showed the basic materials parameters of ZnO.

Table 1.1 The basic materials parameters of wurtzite ZnO [23].

PROPERTIES	VALUES
Lattice parameters at 300 K a_0 c_0 a_0/c_0	0.32495 nm 0.52069 nm 1.602 (1.633 for ideal hexagonal structure)
Density	5.606 g/cm^3
Stable phase at 300 K	Wurtzite
Melting point	1975°C
Linear expansion coefficient (/°C)	$a_0 : 6.5 \times 10^{-6}$, $c_0 : 3.0 \times 10^{-6}$
Thermal conductivity	0.6, 1–1.2
Static dielectric constant	8.656
Refractive index	2.008, 2.029
Energy gap	3.4 eV (direct)
Intrinsic carrier concentration	< 106 /cm^3
Exciton binding energy	60 meV
Electron effective mass	0.24
Electron hall mobility at 300 K for low n-type conductivity	200 cm^2 /V.s
Hole effective mass	0.59
Hole hall mobility at 300 K for low p-type conductivity	5.50cm^2 /V.s

1.1.5 Applications

The applications of ZnO powder are numerous, and the principal ones are summarized below. Most applications exploit the reactivity of the oxide as a precursor to other zinc compounds. For material science applications, ZnO has excellent chemical, electrical and optical properties that find applications as reinforcing filler for elastomer [24], catalyst [3–4], gas sensors and varistor [25], electrode of solar cells [26], photocatalysts [27] and UV attenuating material [28], etc. More recently, various nano-phases of ZnO have exhibited excellent physical and chemical properties different from those of bulk ZnO material [29], especially ZnO nanoparticles, which have been made into a brand new type of photocatalyst with applications in the areas of anti-bacteria, mold prevention, air-ventilation, and water purification [30]. Because of its larger binding exciton energy (about 60 meV, exceeding the room temperature energy of 26 meV), ZnO is also an ideal UV emission material. The mechanisms of UV emission and optical properties in broad range size of ZnO nanoparticles were reported [31], however, the intensity of the UV emission was weak and suppressed by visible emission. One application which has begun to be commercially available is the use of ZnO as the front contact for solar cells or of liquid crystal displays [32]. Transparent thin-film transistors (TTFT) can be produced with ZnO. As field-effect transistors, they even may not need a p-n junction [33], thus avoiding the p-type doping problem of ZnO. Some of the field-effect transistors even use ZnO nanorods as conducting channels [34].

1.1.6 Doping ZnO with a metal

The doping of ZnO with a metal could change its properties; doping with the II elements, (Cd, Mg) may modulate the value of the band gap and increase the UV luminescence intensity [35]. The band gap of ZnO can be tuned via divalent

substitution on the cation site to produce heterostructures. Cd doping can decrease the band gap (to as low as ~3.0 eV), whereas Mg doping can increase the band gap (to as high as ~4.0 eV). Doping with the III elements, (Al, Ga, In) doping could influence electrical properties [36–37], such as electrical resistivity or carrier concentration. Therefore, research on the properties of ZnO nanoparticles doped with different metal elements is of great significance. Aluminium-doped ZnO layers are used as a transparent electrode. The constituents Zn and Al are much cheaper and less poisonous compared to the generally used indium tin oxide (ITO).

1.1.7 ZnO nanostructure

ZnO nanostructures can be synthesized into a variety of morphologies including nanowires, nanorods, tetrapods, nanobelts, nanoflowers, nanoparticles etc. Nanostructures can be obtained with most above-mentioned techniques, at certain conditions, and also with the vapor-liquid-solid method [38]. Meanwhile, some useful techniques for preparing nanoparticles have been developed, such as sol–gel synthesis, laser ablation method, and mechanical milling method [39]. Through the methods above, the size of nanoparticles is distributed within a range between several nanometers to several hundreds of nanometers. Alternatively, FSP is a new method to grow nanoparticles of metal oxide semiconductors with a high melting point [40]. Because the reaction is completed with high temperature, the nanoparticles are uniform in size and produced in large quantity. However, the ZnO nanoparticles doped with some metals have been rarely reported by this method. Thus, the following part would discuss the effects of Nb doping on the applications of ZnO nanoparticles synthesized by FSP.

1.2 Niobium

Nb is a lustrous, grey, ductile, paramagnetic metal in group V of the periodic table (Table 1.2), although it has a typical configuration in its outermost electron shells compared to the rest of the members. (This can be observed in the neighborhood of niobi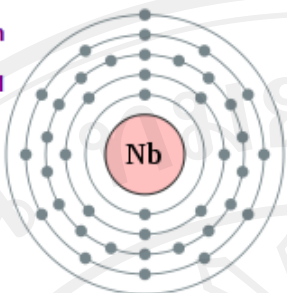um (41), ruthenium (44), rhodium (45), and palladium (46).) Nb becomes a superconductor at cryogenic temperatures. At atmospheric pressure, it has the highest critical temperature of the elemental superconductors: 9.2 K [41]. Nb has the largest magnetic penetration depth of any element [41]. In addition, it is one of the three elemental Type II superconductors, along with vanadium and technetium. The superconductive properties are strongly dependent on the purity of the Nb metal [42]. When very pure, it is comparatively soft and ductile, but impurities make it harder [43]. The metal has a low capture cross-section for thermal neutrons; [44] thus it is used in the nuclear industries [45].

Table 1.2 The electron configuration of vanadium, niobium and tantalum [41].

Z	Element	No. of electrons/shell
23	vanadium	2, 8, 11, 2
41	niobium	2, 8, 18, 12, 1
73	tantalum	2, 8, 18, 32, 11, 2

Figure 1.2 The periodic table [46].

The metal takes on a bluish tinge when exposed to air at room temperature for extended periods [47]. Despite presenting a high melting point in elemental form (2,468 °C), it has a low density in comparison to other refractory metals. Furthermore, it is corrosion resistant, exhibits superconductivity properties, and forms dielectric oxide layers. Nb is slightly less electropositive and more compact than its predecessor in the periodic table, zirconium, whereas it is virtually identical in size to the heavier tantalum atoms, owing to the lanthanide contraction [43]. As a result, Nb's chemical properties are very similar to those for tantalum, which appears directly below Nb in the periodic table [48]. Although its corrosion resistance is not as outstanding as that of tantalum, its lower price and greater availability make Nb attractive for less demanding uses such as linings in chemical plants [43].

Nb is in many ways similar to tantalum and zirconium. It reacts with most nonmetals at high temperatures: niobium reacts with fluorine at room temperature,

with chlorine and hydrogen at 200 °C, and with nitrogen at 400 °C, giving products that are frequently interstitial and nonstoichiometric [43]. The metal begins to oxidize in air at 200 °C [49], and is resistant to corrosion by fused alkalis and by acids, including aqua regia, hydrochloric, sulfuric, nitric and phosphoric acids [40]. Nb is attacked by hydrofluoric acid and hydrofluoric/nitric acid mixtures. Although Nb exhibits all of the formal oxidation states from +5 to -1, in most commonly encountered compounds, it is found in the +5 state [43]. Characteristically, compounds in oxidation state less than 5+ displays Nb-Nb bonding. Niobium forms oxides with the oxidation states +5 (Nb_2O_5), +4 (NbO_2), and +3 (Nb_2O_3) [45], as well as with the rarer oxidation state +2 (NbO) [47]. Most commonly encountered is the pentoxide, precursor to almost all Nb compounds and alloys [49]. Niobates are generated by dissolving the pentoxide in basic hydroxide solutions or by melting it in alkali metal oxides. Examples are lithium niobate ($LiNbO_3$) and lanthanum niobate ($LaNbO_4$). In the lithium niobate is a trigonally distorted perovskite-like structure, whereas the lanthanum niobate contains lone NbO_4^{3-} ions [50]. The layered niobium sulfide (NbS_2) is also known [43].

Doping with different metal cations and anions is possible for semiconductor oxides like TiO_2 and ZnO. Doping Nb into ZnO is quite attractive because there is a valence difference of three between Nb^{5+} and Zn^{2+}, thus each Nb atom can contribute more than one electron to the electrical conductivity [51]. Kudo et al. [52] reported that ZnO and TiO_2 loaded with 1, 5 and 10 wt% Nb_2O_5 enhanced the photo-sensitivity of the electro-conductivity of TiO_2 and ZnO. Nb-doped TiO_2 nanoparticles improved the sensitivity towards CO and ethanol over that of pure TiO_2 were report by Teleki et al. [53] and DSSC devices using undoped TiO_2, 10% Nb-doped TiO_2 and 20% Nb-

doped TiO_2 was fabricated and tested respectively by Siddiki et al. [54]. The results showed that Nb-doped TiO_2 leads to higher device efficiency than the undoped TiO_2.

The basic materials parameters of Nb are shown in Table 1.3

Table 1.3 Physical properties of Nb [55].

Properties	Value
Atomic number	41
Atomic mass	92.91 $g.mol^{-1}$
Melting point	2410 °C
Boiling point	5100 °C
Density	8.4 $g.cm^{-3}$ at 20°C
van der waals radius	0.143 nm
Ionic radius	0.070 nm (+5) ; 0.069 nm (+4)

1.3   Flame spray pyrolysis (FSP)

FSP was other name besides flame aerosol pyrolysis or flame aerosol synthesis. This was a process that used energy source as flame to energized aerosol combustion, generally used hydrogen or methane as fuel gas mixed oxygen in flame reactor. Flame aerosol synthesis refers to the formation of fine particles from gases in flames. Recently, flame aerosol synthesis is used on large scale to produce carbon black, fumed silica and titania pigments. In general, flame synthesis and especially FSP is a fast, cost-effective, and versatile process for the production of a wide variety of difference nanoparticles [8]. FSP is one of the most promising techniques for synthesis of an inorganic nanoparticles such as high quality metal oxide nano-powders and spinels [56], lasing materials [56] nano-ZrO_2 [57], nano-CeO [57], ZnO quantum dots [58], Pt/Al_2O_3 catalysts [59], and even metal alloys [60] that can be

used for catalysts, sensors and electroceramics. The resulting metal oxide powders show a very high surface area together with high material purity. The process further gives the possibility of producing mixed metal oxides with a high homogeneity both in chemical composition and powder particle size.

FSP is a one-step process by which a metal precursor(s), dissolved in a solvent, is sprayed with an oxidising gas into a flame zone where the droplets are combusted and the precursor converted into nano-sized metal or metal-oxides particles, depending on the metal and the operating conditions. This technique is flexible as it allows for the use of a wide range of precursors, solvents and process conditions and thus provides control over particle size and composition. Essentially little is known on how the multicomponent FSP droplets are converted to particles because in situ measurement of the flame and particle characteristics is rather challenging in these droplet-particleladen flames. Such data are needed to understand some of the intriguing FSP results such as the formation of solid or hollow Al_2O_3 by switching the dispersion oxidant gas from oxygen to air [61] and homogeneous or inhomogeneous nano-Bi_2O_3 or CeO_2 by controlling the composition of the FSP precursor solution [62]. Before even this, however, a quantitative understanding the role of droplet evaporation on the solid product particle size is needed for FSP process design and operation. Recently, by accounting for coagulation and sintering during FSP and through neglect of the particle polydispersity and droplet evaporation, a good agreement between the predicted and measured average ZrO_2 particle diameters was obtained [63].

The properties of the nanoparticles can be varied over a large range of morphology and sizes by selecting precursor mixture, flame condition and nozzle parameters. For the flame condition, at a low oxidant flow rates, the specific surface

area increased with increasing oxidant flow rate as the spray flame length was reduced, leading to shorter residence time and allowing less time for particle growth. Using oxygen as oxidant the droplets burn much faster than with air, thus, product particles experience longer residence times at higher temperature [40]. The effect of solution feed rate on particles specific surface area and crystalline size was also investigated [64]. The solution feed rate increased the flame height, and therefore coalescence was enhanced, resulting in large primary particles [64]. Furthermore, the flame conditions can be used to control the morphology of particles. Formulation of liquid precursors is one of the more important steps to FSP particle synthesis. Selection of metal precursors and solvents with suitable combustion enthalpies, melting/decomposition temperatures, miscibility and chemical stability are intrinsic to the overall particles formation in the flame which in turn determine the resultant particle properties. Early formulations of FSP precursors were based on solid nitrates [62] acetates [65] and acetylacetonates [66] as these were natural choices in direct extensions of FSP. While many of these precursors were economical and readily available commercially, they do not always yield the homogeneous morphology comprising of fine and dense particles. The low combustion enthalpy of some of these precursors coupled with their high melting/decomposition points can be disadvantageous, some of these disadvantages can be circumvented by implementing the right processing conditions. The combination of low combustion enthalpy density (<4.7 kJ g^{-1} gas) and higher metal precursor melting/decomposition point relative to the solvent boiling point i.e. T_{bp} (solvent)/ $T_{d/mp}$ (precursor) < 1 during FSP results in the formation of inhomogeneous particles [67]. Under these conditions, both micron- and nanoparticles co-exist due to particle formation through the droplet-to-particle [68] and gas-to-particle routes [8] respectively. The former arises from incompletely

evaporated droplets as in classic spray pyrolysis [69], while the latter from the supersaturation of metal vapor [62]. Hollow particles can even be formed if the metal precursor precipitates at the droplet surface during solvent evaporation. In the case where an impermeable shell is formed, internal pressure build-up during the evaporation of trapped solvent leads to fragmentation of the spherical shells [62]. Subsequent solid-state reactions and densification take place forming micron-sized metal oxides. In the case when FSP is operated at high combustion enthalpy densities, sufficient heat is provided to evaporate the precursor intermediate products to yield homogeneous fine particles, even at T_{bp}(solvent)/$T_{d/mp}$(precursor) < 1.
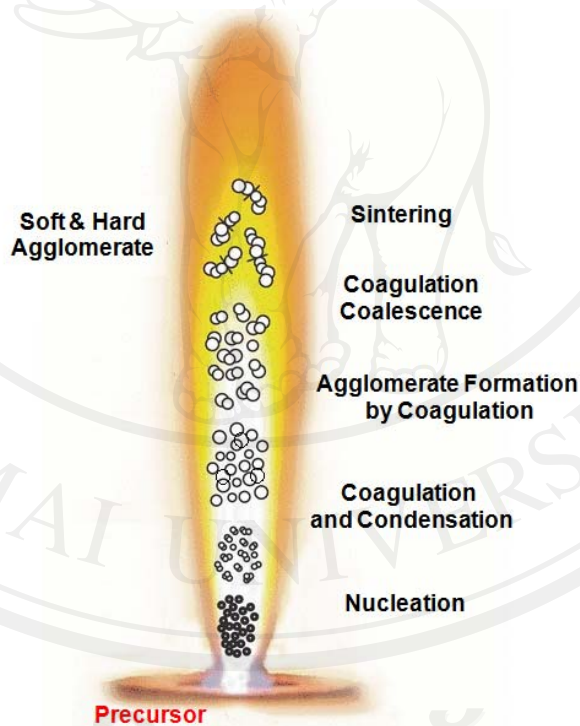

Figure 1.3 Sketch of the basic steps of particle formation and growth by gas-to-particle conversion in FSP flame spray pyrolysis. The liquid precursor mixture is rapidly dispersed by a gas stream and ignited by a premixed methane/oxygen flame. After evaporation and burning of the precursor, particles are formed by nucleation, condensation, coagulation, coalescence.

1.3.1 The basic steps of particle formation and growth by gas-to-particle conversion in FSP

1.3.1.1 Nucleation [70]

Nucleation is the extremely localized budding of a distinct thermodynamic phase. Some examples of phases that may form via nucleation in liquids are gaseous bubbles, crystals or glassy regions. Creation of liquid droplets in saturated vapor is also characterized by nucleation. Nucleation of crystalline, amorphous and even vacancy clusters in solid materials is also important, for example to the semiconductor industry. Most nucleation processes are physical, rather than chemical, but a few exceptions do exist (e.g. electrochemical nucleation). Nucleation normally occurs at nucleation sites on surfaces contacting the liquid or vapor. Suspended particles or minute bubbles also provide nucleation sites. This is called heterogeneous nucleation. Nucleation without preferential nucleation sites is homogeneous nucleation.

Homogeneous nucleation occurs spontaneously and randomly, but it requires superheating or supercooling of the medium. Nucleation is involved in such processes as cloud seeding and in instruments such as the bubble chamber and the cloud chamber. Homogeneous nucleation is the formation of particles from a supersaturated vapor without the assistance of condensation nuclei or ions. This process is also called self-nucleation. This type of particle formation seldom occurs naturally but can be produced readily in the laboratory to study in process of formation and growth. It is covered here because it serves as a framework for understanding the more common heterogeneous nucleation processes covered in nucleated condensation.

1.3.1.2 Nucleated condensation [70]

Condensation and Evaporation, the formation and growth of aerosol particles by condensation is the principal method of aerosol production in nature and

the most important mass transfer process between the gas phase and the particles phase. This process usually requires a supersaturated vapor and is initiated by the presence of small particles (nuclei) or ions that serve as sites for particle formation. The supersaturation for the formation of atmospheric clouds is produced by cooling a saturated vapor by mixing or adiabatic expansion. The supersaturation for the formation of photochemical smog is produce by gas-phase chemical reactions that yield products of low vapor pressure.

The opposite of the condensation growth process is the closely related process of evaporation. This process is important for spray-drying applications and is involved in the production of nuclei, such as sea salt nuclei, which are originally formed as droplets and evaporate to form nuclei that serve as sites for subsequent condensation.

Nucleated condensation or heterogeneous nucleation is a process of particle formation and growth that is promoted by the presence of condensation nuclei or ions. Whereas homogeneous nucleation usually requires saturation ratios of 2–10, nucleated condensation can occur at supersaturations of only a few percent. In the case of soluble nuclei, condensation can occur in saturated conditions and size-stable droplets can be formed. Nucleated condensation is the primary mechanism for cloud formation in the atmosphere.

1.3.1.3 Coagulation [70]

Coagulation theory of aerosols nanoparticles

Coagulation of aerosols might be result of Brownian motion and external force that fabricated their relative motion. Important external force was gravity, electrical force as well aerodynamic effect. These factors directly affected with aerosol that

varied with aerosol number as well as continuously decreased when number concentration decreased also.

Aerosol coagulation caused by Brownian motion called Brownian coagulation. Brownian motion was spontaneous and always presented for suspension of particle both in liquid as well as gas. Determination of this motion caused by surrounding molecule collided particles in all direction that affected particle had random movement. Brownian motion was excellently by molecular kinetic theory of heat as works of Albert Einstein in 1905. This theory, based on classical mechanics, helped to explain the behavior of what were known as colloidal solution, a behavior of which had been studied by Svedberg, Perrin, Zsigmondy and countless other scientists within the context of what had grown into a large branch of science, colloid chemistry [71]

Aerosol coagulation caused by external forces such as gravity, electrical forces or from aerodynamic effects totally called kinematic coagulation. In horizontal movement, large particles might use more energy than small particle for created same velocity. Thus particles obtained same driving energy, large particle for created same velocity but same kinetic energy. In vertical movement, particles were restrained by gravity. Large particle that had low velocity was caused easily stop by gravity. These particles still behaved in line with Newton's law, higher initial velocity particles could obtain more height. Difference of these particles velocity created relative velocity that leaded to collision and coagulation that was called gravitational coagulation.

Furthermore, electrostatic coagulation was called when change particles caused collision that could experience either attraction or repulsion. And particles moved to pass through surrounding air, flow field in fluid was turbulent then

leaded to collision between neighboring particles by two mechanisms. First, spatial variation of turbulent motion was called shear mechanism. Second, inertia of unequal size particles caused relative velocity was called accelerative mechanism.

1.3.1.4 Coalescence [72]

Coalescence is the formation of one elliptic particle from two powder grains under the effect of temperature and surface tension. Grain coalescence is observed in most systems. Contacts form after the liquid appears and there is a small probability that the contact will have a low-angle grain boundary that allows coalescence. Alternatively, for grains with differing sizes, the driving force for coalescence is boundary migration due to curvature, which suggests that coalescence is favored at the large-small grain contacts. Other causes of coalescence are gradients in chemistry or strain state. The grain size grows by coalescence while the number of grains decreases continuously.
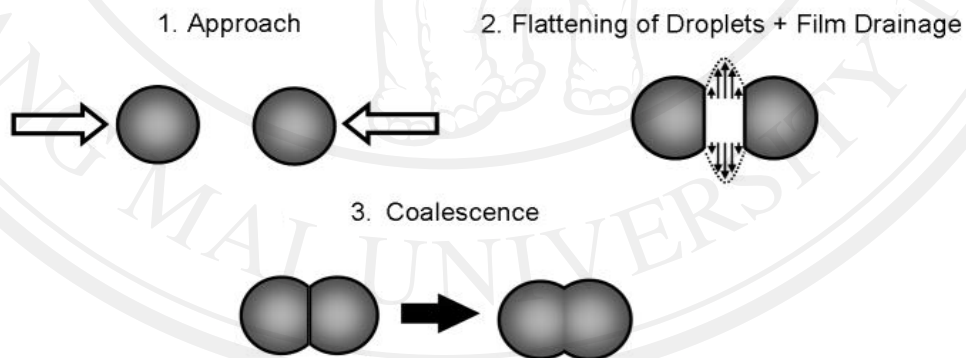

Figure 1.4 Steps leading to grain growth by coalescence of small and large grains with a curved grain boundary.
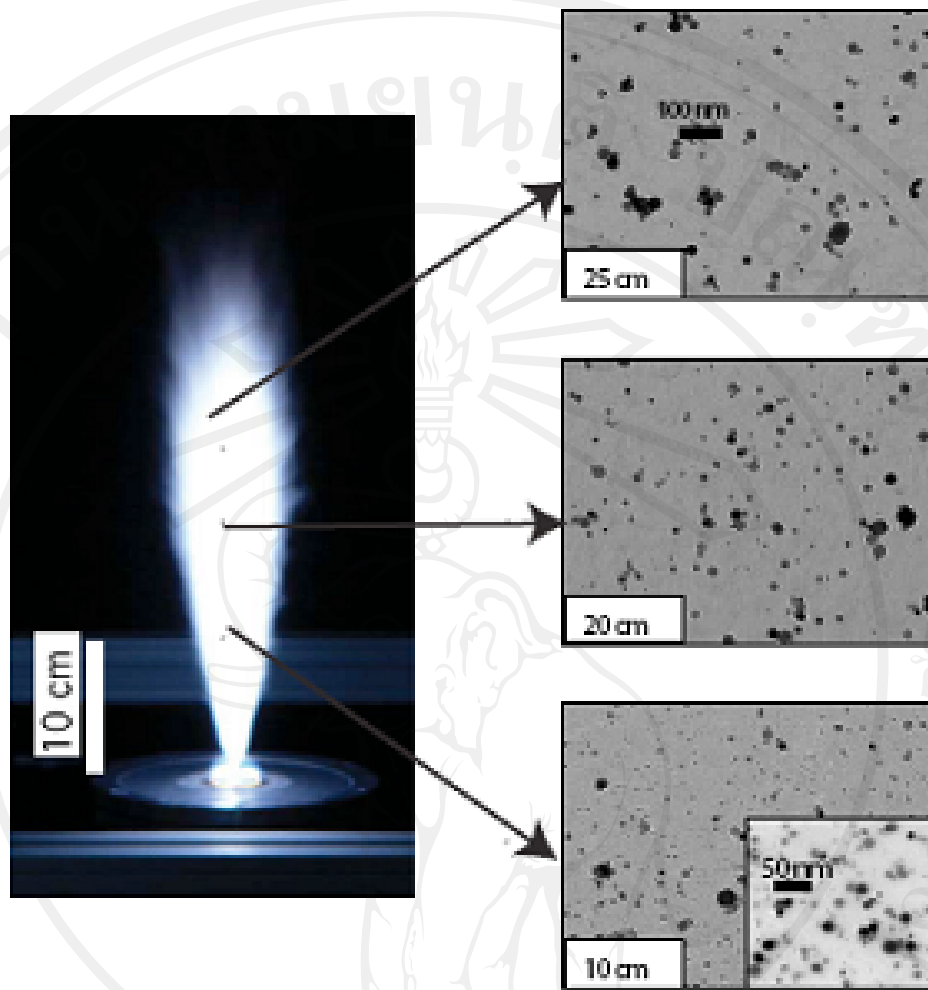
Figure 1.5 Image of a lab-scale reactor (right). The critical sub-processes in the FSP process and their approximate spatial location are indicated on the left. Nanoparticle samples extracted from the flame at the indicated heights are shown [72].

The vapor-phase processes have a tendency to form agglomorates rather than the required spherical particles. This occurs when the characteristic sintering (coalescence) (Figure 1.5) time is greater than characteristic time for particle-particle collisions. Sintering is a method by which nanoparticles coalescence to assume, larger and more uniform (tending towards spheres) particles.

1.4 The theory of characterization techniques

The nanopowders that were investigated in this study were characterized using X-ray diffraction (XRD), Brunaure-Emmett-Teller (BET) analysis, transmission electron microscopy (TEM), scanning electron microscopy (SEM), energy dispersive X-ray spectroscopy (EDS), UV-vis spectroscopy and Atomic Force Microscopy (AFM). The theory of these characterization techniques can be found in the following sections.

1.4.1 X-ray diffraction method [73–75]

X-ray diffraction (XRD) is a standard tool for identification of crystalline phases in powder samples. The crystalline phase in the sample diffracts X-ray according to Bragg's equation (Equation 1.1) as follow $n\lambda = 2d_{hkl} \sin\theta_{hkl}$ [73] which relates lattice spacing to the wavelength of the X-ray. The amount of sample needed in practice is roughly 100 mg or more. Crystalline phases present at levels of about 1 percent or greater can be detected. The unit cell dimension (a, b ,c) of the crystal can also be determined and provide more information for complex structure materials. Amorphous materials are not observed. In routine work, XRD relies on availability of standards that allow identification of peaks in the diffraction pattern.

1.4.1.1 Crystal structure [74]

Solid matter consists out of two types of material: amorphous and crystalline. In an amorphous sample the atoms are arranged in a random way (similar to what we find in a liquid). Glasses are an example of amorphous materials. In a crystalline sample the atoms are arranged in a regular or ordered pattern and there is a smallest volume element that, by repetition in three dimensions, can describe the crystal (just like a brick wall can be described by the shape and orientation of a single brick). This smallest volume element is called a unit cell. The dimensions of this unit cell can be

described by three axes namely: a, b and c and the angles between the axis are α, β and γ. A schematic diagram of the unit cell is given in Figure 1.6
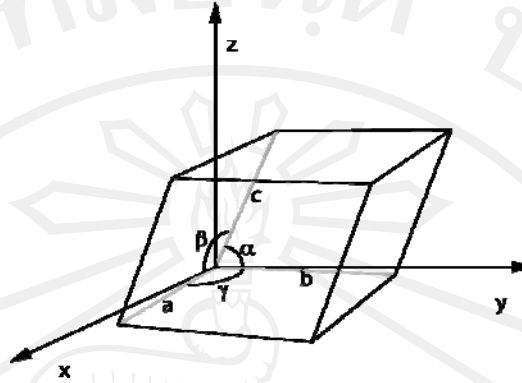

Figure 1.6 A unit cell from a three dimensional lattice [74].

About 95% of all solid materials can be described as crystalline. When X-ray interacts with a crystalline substance a diffraction pattern is formed. This pattern of a pure substance is therefore acting as a fingerprint of that substance. The powder diffraction method is used for identification and characterization of polycrystalline phases

When an electron is placed in an alternating electromagnetic field, it will oscillate with the same frequency as the field. The electrons around an atom will start to oscillate with the same frequency as the incoming beam when an X-ray beam hits the atom. Destructive interference will be found in almost all the directions, that is the combining waves is out of phase and there will be no resultant energy leaving the sample. The atoms in a crystal are however arranged in an ordered way and constructive interference will therefore occur in a very few directions. These waves will be in phase and there will be well defined X-ray beams leaving the sample at various directions. A diffracted beam may be therefore described as a beam composed of a large number of scattered rays mutually reinforcing one another.

This model is very complex to handle mathematically and it is preferred to talk about X-ray reflections from a series of parallel planes inside the crystal. The Miller indices h, k, l define the orientation and interplanar spacings of these planes. The a axis of the unit cell will be cut into h sections, the b axis into k sections and the c axis into l sections by a given set of planes with indices h, k, l. When the planes are parallel to the corresponding axis it is indicated by a zero.

1.4.1.2 Bragg's Law

Bragg's law is the basis of XRD analysis. With this law it is possible to make accurate quantifications of experimental results in the determination of crystal structures. The law was derived by English physicist Sir W.H. Bragg and his son Sir W.L. Bragg in 1913. It was used to explain why the cleavage faces of crystals appear to reflect X-ray beams at certain angles of incidence.
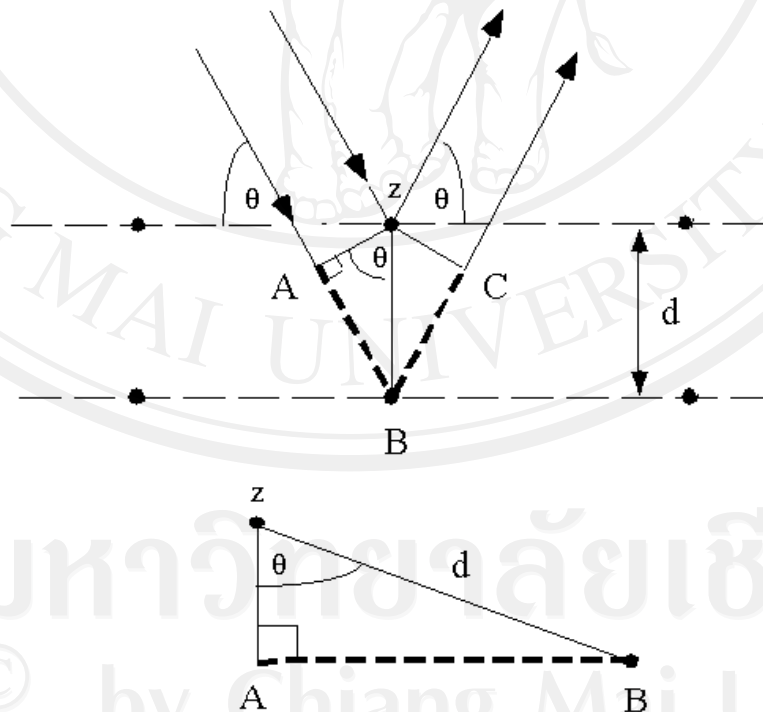

Figure 1.7 Deriving Bragg's law using the reflection geometry and applying trigonometry [75].

The lattice planes in the simple crystal in Figure 1.9 are separated by a distance d. Bragg's law is given by

$$n\lambda = 2d_{hkl} \sin \theta_{hkl} \qquad (1.1)$$

where:

d_{hkl} = interplanar distance between (hkl) planes,

n = order of diffraction,

λ = wavelength of incident X-rays (e.g. 1.542 Å for copper K_α X-rays).

The angle between the transmitted and diffracted beams will always be equal to 2θ because of the geometry of the Bragg's condition. This angle can be obtained readily in experimental situations and the results of X-ray diffraction are therefore given in terms of 2θ. It is however very important to remember that the angle that is used in the Bragg's equation must correspond to the angle between the incident radiation and the diffracting plane, i.e. θ.

1.4.1.3 Crystallinity

In contrast to a crystalline pattern consisting of a series of sharp peaks, amorphous materials (liquids, glasses etc.) produce a broad background signal. Many polymers show semicrystalline behavior, *i.e.* part of the material forms an ordered crystallite by folding of the molecule. One and the same molecule may well be folded into two different crystallites and thus form a tie between the two. The tie part is prevented from crystallizing. The result is that the crystallinity will never reach 100%. Powder XRD can be used to determine the crystallinity by comparing the integrated intensity of the background pattern to that of the sharp peaks. Values obtained from

powder XRD are typically comparable but not quite identical to those obtained from other methods such as DSC.

1.4.1.4 Lattice parameters

The position of a diffraction peak is independent of the atomic positions within the cell and entirely determined by the size and shape of the unit cell of the crystalline phase. Each peak represents a certain lattice plane and can therefore be characterized by a Miller index. If the symmetry is high, e.g. cubic or hexagonal it is usually not too hard to identify the index of each peak, even for an unknown phase. This is particularly important in solid-state chemistry, where one is interested in finding and identifying new materials. Once a pattern has been indexed, this characterizes the reaction product and identifies it as a new solid phase. Indexing programs exist to deal with the harder cases, but if the unit cell is very large and the symmetry low (triclinic) success is not always guaranteed.

1.4.1.5 Powder Diffraction and identification of phases by XRD

Powder XRD (X-ray Diffraction) is perhaps the most widely used X-ray diffraction technique for characterizing materials. As the name suggests, the sample is usually in a powdery form, consisting of fine grains of single crystalline material to be studied. The technique is used also widely for studying particles in liquid suspensions or polycrystalline solids (bulk or thin film materials).

The term 'powder' really means that the crystalline domains are randomly oriented in the sample. Therefore when the 2–D diffraction pattern is recorded, it shows concentric rings of scattering peaks corresponding to the various d spacings in the crystal lattice. The positions and the intensities of the peaks are used for identifying the underlying structure (or phase) of the material. A powder XRD scan

from a FeOOH sample is shown in Figure 1.8 as a plot of scattering intensity vs. the scattering angle 2θ or the corresponding d-spacing. The peak positions, intensities, widths and shapes all provide important information about the structure of the material.
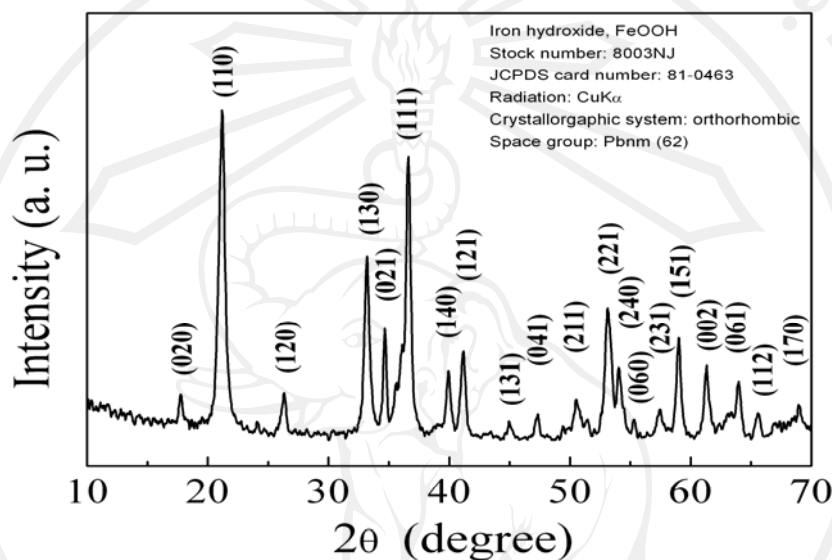

Figure 1.8 XRD pattern of FeOOH sample [75].

After a scan of the sample the X-ray intensity can be plotted against the angle θ (usually reported as 2θ because of the way older diffractometers were made) to produce a chart, like the one shown here. The angle 2θ for each diffraction peak can then be converted to d-spacing, using the Bragg equation. One can then work out the crystal structure and associate each of the diffraction peaks with a different atomic plane in terms of the Miller Index for that plane (hkl). A group known as the Joint Committee on Powder Diffraction Standards (JCPDS) has collected data such as this on thousands of crystalline substances. This data can be obtained as the JCPDS Powder Diffraction File. Since every compound with the same crystal structure will

produce an identical powder diffraction pattern, the pattern serves as kind of a "fingerprint" for the substance, and thus comparing an unknown mineral to those in the Powder Diffraction file enables easy identification of the unknown.

Figure 1.9 X-ray diffraction system used in this research.

1.4.2 Brunauer-Emmett-Teller (BET) analysis–Particle size (d_{BET}) [76]

Surface areas of powders are usually measured using nitrogen or helium adsorption followed by analysis of the data using the BET isotherm. Estimates of surface areas provide information about the porosity of particles and the primary particle size in particles that consist of agglomerates of smaller particles. The primary particle size can be related to surface area assuming that the particles are smooth monodisperse spheres. Specific surface areas can range from a few m^2/g to hundreds of m^2/g in the case of highly porous materials or very fine particles.

In an experiment, the BET method uses the adsorption of nitrogen on the particle surface and the measurement is operating at low, constant temperature (boiling point of liquid nitrogen at around -200ºC). This method was introduced by

Brunauer et al. [76]. Increasing the partial pressure over a particle sample the uptake of nitrogen by the sample is measured. Following the IUPAC classification and assuming that the measured particle samples have the type II or IV which means that they are mesoporous (pores are in the size range of 2 nm to 50 nm) or even microporous (pores larger than 50 nm) only monolayer of adsorptive nitrogen is built up at the surface by increasing the partial pressure. Knowing the amount of adsorbed nitrogen and assuming that there is only one monolayer a specific surface area (SSA_{BET}) of metal oxide and metal-doped metal oxide particles can be calculated. To calculate the mean particle diameter or as well called sauter mean diameter (d_{BET} =d_{SMD}) by assuming that the particles do have spherical shape the following Equation 1.2 is used:

$$d_{BET} = \frac{6}{SSA_{BET}\rho_{sample}}$$ (1.2)

1.4.3 Scanning Electron Microscope (SEM) [77–80]

The scanning electron microscope (SEM) uses a focused beam of high-energy electrons to generate a variety of signals at the surface of solid specimens. The signals that derive from electron-sample interactions reveal information about the sample including external morphology (texture), chemical composition, and crystalline structure and orientation of materials making up the sample. In most applications, data are collected over a selected area of the surface of the sample, and a 2–dimensional image is generated that displays spatial variations in these properties. Areas ranging from approximately 1 cm to 5 microns in width can be imaged in a scanning mode using conventional SEM techniques (magnification ranging from 20X to approximately 30,000X, spatial resolution of 50 to 100 nm). The SEM is also capable

of performing analyses of selected point locations on the sample; this approach is especially useful in qualitatively or semi-quantitatively determining chemical compositions (using EDS), crystalline structure, and crystal orientations (using EBSD). The design and function of the SEM is very similar to the EPMA and considerable overlap in capabilities exists between the two instruments [77].

During SEM analysis, a beam of electrons is focused on a spot volume of the specimen. The electron beam has energies that range from a few keV to 50 keV and it is focused by two condenser lenses into a beam with a very fine spot size. This beam then passes through the objective lens, where pairs of coils deflect the beam either linearly or in a raster fashion over a rectangular area of the sample surface (Figure 1.10).

When the primary electron beam strikes the surface of the sample it is scattered by atoms in the sample. Through this scattering event, the primary beam spreads effectively and fills a teardrop-shaped volume (Figure 1.11), known as the interaction volume, and this extends about 1 to 5 μm into the surface. Secondary electrons are emitted from interactions in this region, they are then detected, converted to a voltage and amplified to produce an image. More than one type of signal can be produced by SEM and they include secondary electrons, back-scattered electrons (BSEs), characteristic X-rays, cathodoluminescence, specimen current and transmitted electrons. Specialized detectors are required for the detection of these signals and they are usually not all present on a single machine [78].
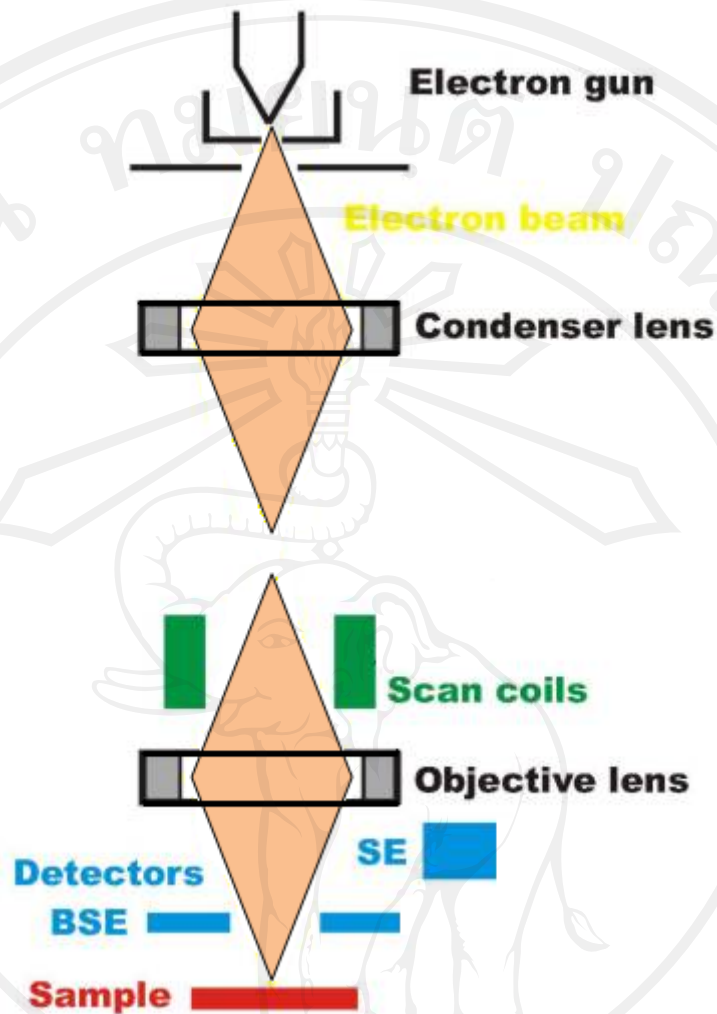
Figure 1.10 Schematic diagram of a typical SEM [79].

Sample preparation can be minimal or elaborate for SEM analysis, depending on the nature of the samples and the data required. Minimal preparation includes acquisition of a sample that will fit into the SEM chamber and some accommodation to prevent charge build-up on electrically insulating samples. Most electrically insulating samples are coated with a thin layer of conducting material, commonly carbon, gold, or some other metal or alloy. The choice of material for conductive coatings depends on the data to be acquired: carbon is most desirable if elemental analysis is a priority, while metal coatings are most effective for high resolution

electron imaging applications. Alternatively, an electrically insulating sample can be examined without a conductive coating in an instrument capable of "low vacuum" operation. Figure 1.12. shows SEM system used in this research.
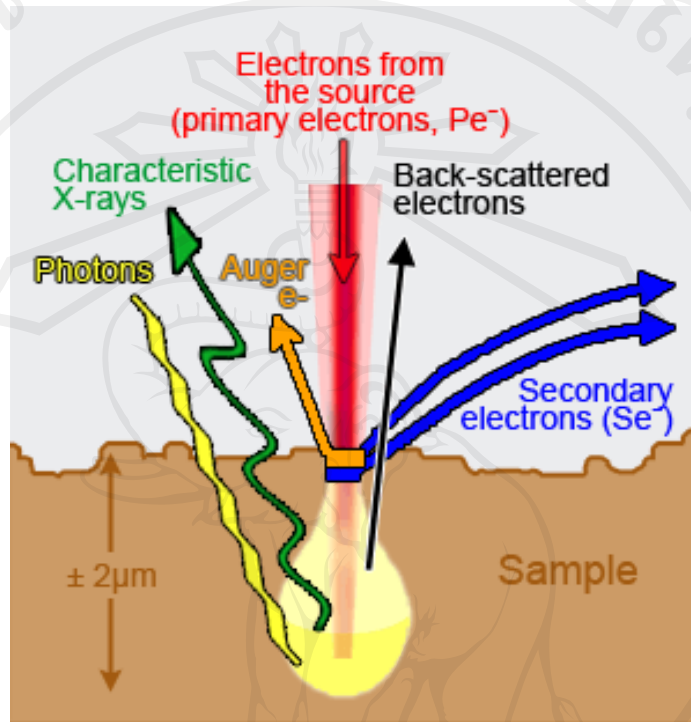

Figure 1.11 Electrons produced in SEM [80].

Figure 1.12 SEM system used in this research.

1.4.4 Energy Dispersive X-ray Spectroscopy (EDS) [81–82]

Interaction of an electron beam with a sample target produces a variety of emissions, including X-rays. An energy-dispersive (EDS) detector is used to separate the characteristic X-rays of different elements into an energy spectrum, and EDS system software is used to analyze the energy spectrum in order to determine the abundance of specific elements. EDS can be used to find the chemical composition of materials down to a spot size of a few microns, and to create element composition maps over a much broader raster area. Together, these capabilities provide fundamental compositional information for a wide variety of materials.

EDS systems are typically integrated into either an SEM or EPMA instrument. EDS systems include a sensitive X-ray detector, a liquid nitrogen dewar for cooling, and software to collect and analyze energy spectra. The detector is mounted in the sample chamber of the main instrument at the end of a long arm, which is itself cooled by liquid nitrogen. The most common detectors are made of Si(Li) crystals that operate at low voltages to improve sensitivity, but recent advances in detector technology make available so-called "silicon drift detectors" that operate at higher count rates without liquid nitrogen cooling. An EDS detector contains a crystal that absorbs the energy of incoming X-rays by ionization, yielding free electrons in the crystal that become conductive and produce an electrical charge bias. The X-ray absorption thus converts the energy of individual X-rays into electrical voltages of proportional size; the electrical pulses correspond to the characteristic X-rays of the element. A typical EDS spectrum is portrayed as a plot of X-rays counts vs. energy (in keV). Energy peaks correspond to the various elements in the sample. Generally they are narrow and readily resolved, but many elements yield multiple peaks. For

example, iron commonly shows strong K_α and K_β peaks. Elements in low abundance will generate X-ray peaks that may not be resolvable from the background radiation.

The chemical composition of the synthesized powders used in this research study was determined by EDS analysis. EDS is an analytic technique and is used for elemental analysis or chemical composition of a sample. When a sample is bombarded with electrons it can emit X-rays, which can be analyzed. By measuring the intensity distribution and energy of the signal generated by a focused electron beam imprinting on a sample, the chemical analysis of the sample can be obtained. The source of the electron beam is the electron gun of a scanning electron microscope.

To stimulate a measurable response from a beam of X-rays into the sample to be characterized. At rest, an atom within the sample contains ground state or "unexcited" electrons, situated in probability shells around the nucleus. The incident beam, however, excites an electron in an inner shell, prompting its ejection and resulting in the formation of a hole within the atom's electronic structure. An electron from an outer, higher energy shell then fills the hole. The release of x elements; thus, by analyzing the x [83].

1.4.5 Transmission electron microscopy and diffraction [84–85]

Transmission electron microscopy (TEM) is a microscopy technique whereby a beam of electrons is transmitted through a very thin sample and interacting with the sample as it passes through. The interaction of the electrons transmitted magnified and then focused onto a fluorescent screen or it can be detected by a camera. The imaging capability of TEMs has a significantly higher resolution than that of light microscopes, because of the small de Broglie wavelength of electrons. The instrument

is therefore enabled to examine fine detail-even as small as a single layer of atoms. TEM is used in a range of scientific fields as a major analysis method, in both biological and physical sciences. Applications of TEM are in material science, pollution and semiconductor research, virology, and cancer research.

The operation of the TEM requires an ultra high vacuum and a high voltage (300 kV). The electrons are emitted by a source and then it is focused and magnified by a set of magnetic lenses (Figure 1.13). The imaged that is formed is either shown on a fluorescent screen or on a monitor and it is printed on photographic film. The resolution power is usually restrained by the technique with which the preparation was achieved and the quality of the lens system. Today's transmission electron microscopes offer resolutions up to 0.1 nm at 300 kV and probe diameters up to 0.34 nm.

TEM exploits three different interactions of electron beam-specimen; unscattered electrons (transmitted beam), elastically scattered electrons (diffracted beam) and inelastically scattered electrons. Different types of images are obtained in TEM, using the apertures properly as well as the different types of electrons. As a result, diffraction patterns are shown because of the scattered electrons. If the unscattered beam is selected, we obtain the Bright Field Image. Dark Field Images are attained if diffracted beams are selected by the objective aperture [84]. Figure 1.13 shows a schematic diagram of the layout of a typical TEM. Figure 1.14 shows the TEM system used in this research.
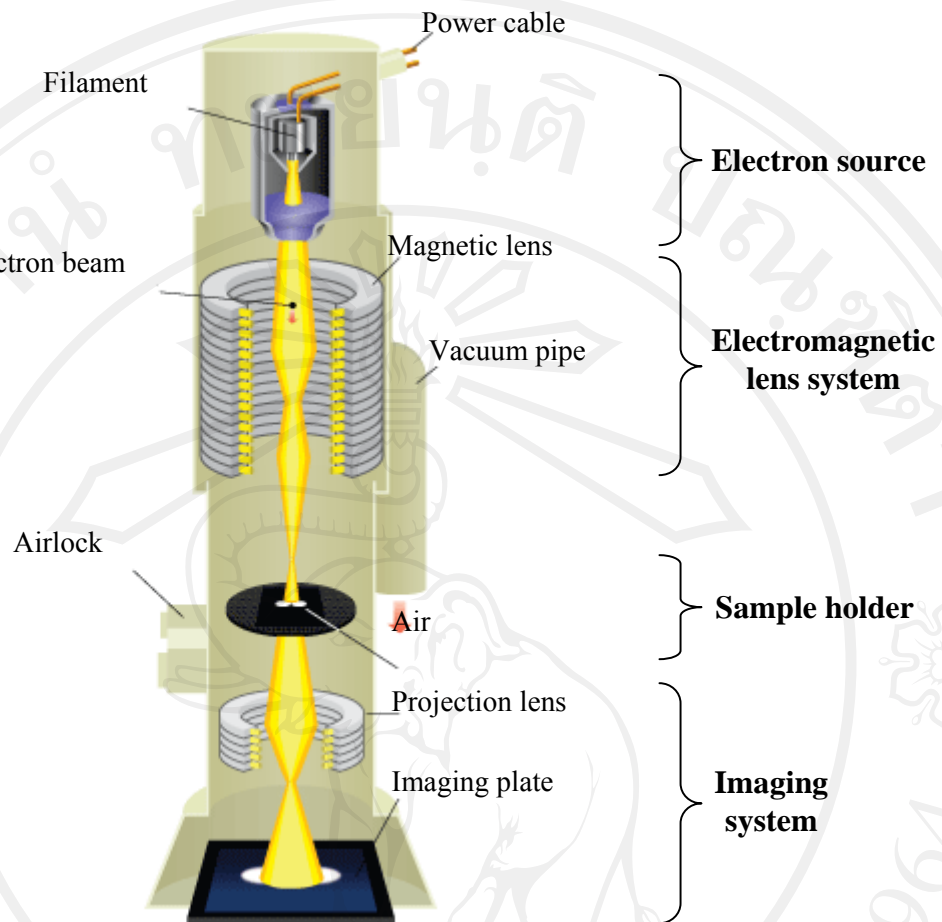
Figure 1.13 Schematic diagram of a TEM [85].

Figure 1.14 TEM system used in this research.

1.4.6 UV-vis absorption spectroscopy [86–89]

Several processes are possible when a sample is stimulated by the application of an external electromagnetic radiation source. The radiation can for example be reflected or scattered. What is important is that some of the radiation can be absorbed and promote some of the sample into the excited state (Figure 1.15). In absorption spectroscopy the amount of light that is absorbed is measured as a function of wavelength. Both qualitative and quantitative information can be obtained from the sample using this method.

Every molecular species is capable of absorbing its own characteristic frequencies of electromagnetic radiation. In this process energy is transferred to the molecule and results in a decrease in the intensity of the electromagnetic radiation that is incident on the sample. The radiation is thus attenuated because of absorption. The Beer–Lambert law or just Beer's law (absorption law) is quantitatively giving how the amount of attenuation depends on the concentration of the absorbing molecule as well as the path length over which the absorption occurs. When light traverses through a medium that contains an absorbing analyte, intensity decreases will occur when the analyte becomes excited. For a sample with a certain concentration, the longer the path length of the light (length of the medium through which the light passes), the more absorbers will be in the path and the greater the attenuation. Also, for a given path length, the higher the concentration of the absorbers the stronger the attenuation of the light beam.
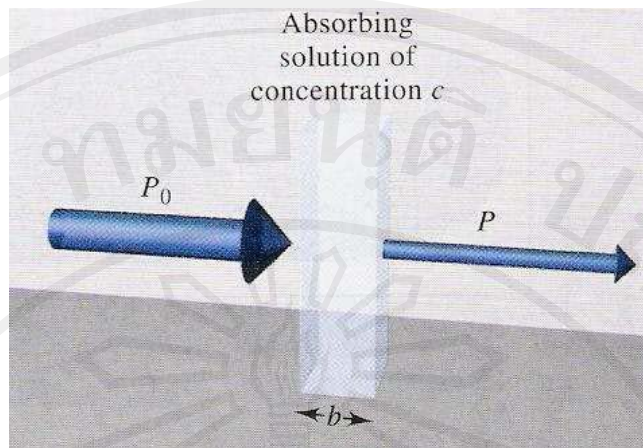
Figure 1.15 Attenuation of a beam of radiation by an absorbing solution. The larger arrow on the incident beam signifies a higher radiant power than is transmitted by the solution. The path length of the solution is b, and the concentration is c [86].

Figure 1.15 is a schematic diagram showing the attenuation of a parallel beam of monochromatic radiation passing through an absorbing solution of thickness b centimeters and a concentration of c moles per liter. The interactions between the photons and absorbing particles cause the radiant power of the beam to decrease from P_0 to P. The fraction of incident radiation transmitted by the solution is the transmittance T of the solution, as shown in equation 1.3. Transmittance is often expressed as a percentage called the percent transmittance.

$$T = \frac{P}{P_0} \tag{1.3}$$

The absorbance A of a solution is translated to the transmittance in a logarithmic manner, as shown in equation 1.4. When the absorbance of a solution increases the transmittance will decrease.

$$A = -\log T$$

$$= -\log\frac{P_0}{P} \qquad (1.4)$$

1.4.6.1 Beer's Law

Absorbance is directly proportional to the concentration of the absorbing species c and to the path length b of the absorbing medium, according to Beer's law. This is expressed by equation 1.5.

$$A = \log\frac{P_0}{P}$$

$$= abc \qquad (1.5)$$

With as a proportionally constant called the absorptivity. Absorbance is a unit less quantity so the units of the absorptivity must cancel the units of b and c. If b has the units of cm and c have the units of mol L^{-1}, then absorptivity must have the units of L g^{-1} cm^{-1}. When b is expressed in cm and the concentration in moles per liter, the proportionality is called the molar absorptivity and is given the special symbol, ε. Thus

$$A = \varepsilon bc \qquad (1.6)$$

where ε has the units of L mol^{-1} cm^{-1} [87].

1.4.6.2 Tauc's relation

The band gap of the powder samples can be determined using Tauc's relation [88]. This is a direct relation between the measured energy and the band gap. Figure 1.16 shows a schematic diagram of the absorption process that takes place in a double beam UV-vis spectrophotometer.
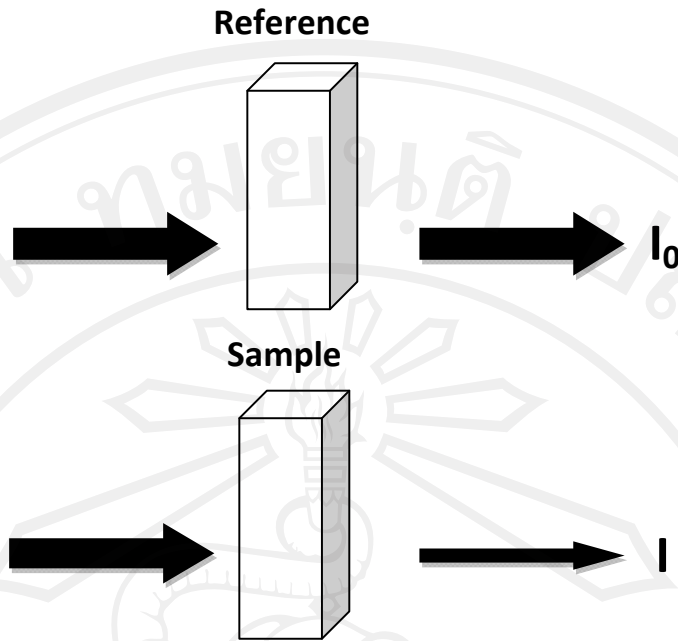
Reference

Sample

Figure 1.16 Schematic diagram of the absorption process.

In Figure 1.16 the intensity of the beam that is measured after it had passed through the reference is referred to as I_0 and the measured intensity of the beam passing through the sample is I. The relation between I and I_0 is given by equation 1.7

$$I = I_0 e^{(-\alpha x t)} \tag{1.7}$$

where α is the absorption coefficient, x is the concentration and t is the path length of the cuvette (10 mm in this case). Equation 1.8 can be rewritten in this form

$$\frac{I}{I_0} = e^{(-\alpha x t)} \tag{1.8}$$

By taken logs on both sides of equation 1.9 it can be rewritten as

$$\log\left(\frac{I}{I_0}\right) = -\alpha x t \tag{1.9}$$

and by making α the subject of the formula a relation for the absorption coefficient can be found in terms of known parameters. This relation is given in equation 1.10

$$\alpha = -\frac{1}{xt}\log\left(\frac{I}{I_0}\right)$$

$$= \frac{1}{xt}\log\left(\frac{I_0}{I}\right) \tag{1.10}$$

The absorbance that is measured with the equipment is equal to $\frac{1}{xt}\log\left(\frac{I_0}{I}\right)$. It is also equal to the absorption coefficient, so the absorption coefficient is therefore equal to the measured absorbance and can be used directly in Tauc's relation without any conversion. Tauc's relation [89] is given by

$$(\alpha h\nu) = (h\nu - E_g)^n$$

$$(\alpha h\nu)^{1/n} \approx (h\nu - E_g) \tag{1.11}$$

where α is the absorption coefficient, hν is the photon energy and E_g is the band-gap of the material. *n* indicates the type of transition. The value of n for allowed direct, allowed indirect, forbidden direct and forbidden indirect transitions are 1/2, 2, 3/2, and 3 [89]. When $(\alpha h\nu)^{1/n} \approx 0$ then $0 \approx h\nu\text{-}E_g$ and this means that $h\nu \approx E_g$ $h\nu \approx E_g$. From this it can be seen that by extrapolating the linear portion of the graph and making $(\alpha h\nu)^{1/n} \approx 0$ the band gap of the material can be obtained.
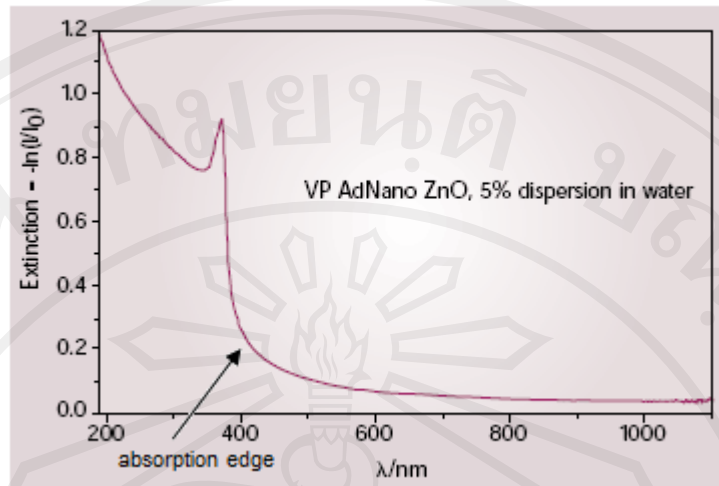
Figure 1.17 UV-vis spectrum of nanostructured zinc oxide [89].

Absorption and percentage transmittance measurements were performed on the powders using a UV-vis absorption spectrophotometer (Figure 1.18).

Figure 1.18 Varian Cary 50 UV-vis absorption spectrophotometer.

1.4.7 Atomic Force Microscopy (AFM) [90−93]

Atomic force microscopy (AFM) is a very high-resolution type of scanning probe microscopy, with demonstrated resolution on the order of fractions of a nanometer, more than 1000 times better than the optical diffraction limit. The AFM is one of the foremost tools for imaging, measuring, and manipulating matter at the nanoscale. The information is gathered by "feeling" the surface with a mechanical probe.
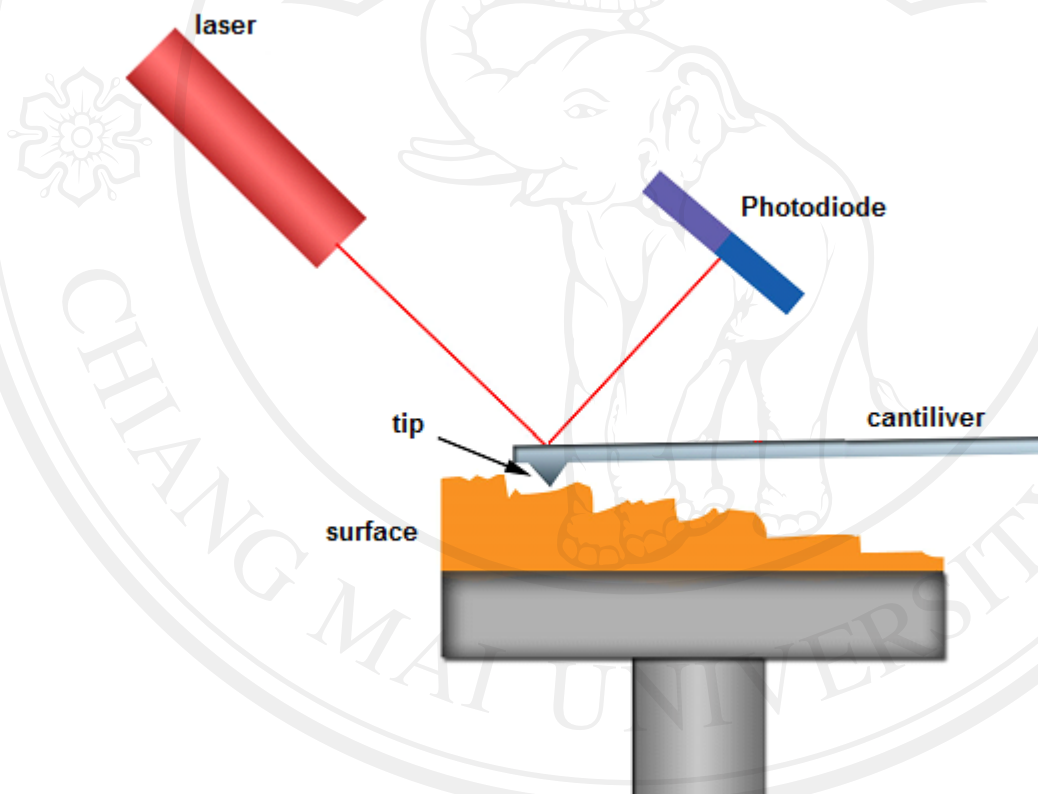

Figure 1.19 Drawing of basic principle of AFM. A cantilever, with a very small tip (probe), moves along the surface and experiences atomic forces. Laser and Photodiode are used to measure those forces [90].

1.4.7.1 Basic principles

The AFM consists of a cantilever with a sharp tip (probe) at its end that is used to scan the specimen surface. The cantilever is typically silicon or silicon nitride with a tip radius of curvature on the order of nanometers. When the tip is brought into proximity of a sample surface, forces between the tip and the sample lead to a deflection of the cantilever according to Hooke's law. Depending on the situation, forces that are measured in AFM include mechanical contact force, van der Waals forces, capillary forces, chemical bonding, electrostatic forces, magnetic forces (see magnetic force microscope, MFM), Casimir forces, solvation forces, etc. Along with force, additional quantities may simultaneously be measured through the use of specialized types of probe (see scanning thermal microscopy, scanning joule expansion microscopy, photothermal microspectroscopy, etc.). Typically, the deflection is measured using a laser spot reflected from the top surface of the cantilever into an array of photodiodes. Other methods that are used include optical interferometry, capacitive sensing or piezoresistive AFM cantilevers. These cantilevers are fabricated with piezoresistive elements that act as a strain gauge. Using a Wheatstone bridge, strain in the AFM cantilever due to deflection can be measured, but this method is not as sensitive as laser deflection or interferometry.

If the tip was scanned at a constant height, a risk would exist that the tip collides with the surface, causing damage. Hence, in most cases a feedback mechanism is employed to adjust the tip-to-sample distance to maintain a constant force between the tip and the sample. Traditionally, the sample is mounted on a piezoelectric tube, that can move the sample in the z direction for maintaining a constant force, and the x and y directions for scanning the sample. Alternatively a 'tripod' configuration of three piezo crystals may be employed, with each responsible

for scanning in the x, y and z directions. This eliminates some of the distortion effects seen with a tube scanner. In newer designs, the tip is mounted on a vertical piezo scanner while the sample is being scanned in x and y using another piezo block. The resulting map of the area $s = f(x, y)$ represents the topography of the sample.

The AFM can be operated in a number of modes, depending on the application. In general, possible imaging modes are divided into static (also called contact) modes and a variety of dynamic (or non-contact) modes where the cantilever is vibrated

1.4.7.2 Imaging modes

The primary modes of operation for an AFM are static mode and dynamic mode. In static mode, the cantilever is "dragged" across the surface of the sample and the contours of the surface are measured directly using the deflection of the cantilever. In the dynamic mode, the cantilever is externally oscillated at or close to its fundamental resonance frequency or a harmonic. The oscillation amplitude, phase and resonance frequency are modified by tip-sample interaction forces. These changes in oscillation with respect to the external reference oscillation provide information about the sample's characteristics.

Contact mode

In the static mode operation, the static tip deflection is used as a feedback signal. Because the measurement of a static signal is prone to noise and drift, low stiffness cantilevers are used to boost the deflection signal. However, close to the surface of the sample, attractive forces can be quite strong, causing the tip to "snap-in" to the surface. Thus static mode AFM is almost always done in contact where the overall force is repulsive. Consequently, this technique is typically called "contact

mode". In contact mode, the force between the tip and the surface is kept constant during scanning by maintaining a constant deflection

Non-contact mode

In this mode, the tip of the cantilever does not contact the sample surface. The cantilever is instead oscillated at a frequency slightly above its resonance frequency where the amplitude of oscillation is typically a few nanometers (<10 nm). The van der Waals forces, which are strongest from 1 nm to 10 nm above the surface, or any other long range force which extends above the surface acts to decrease the resonance frequency of the cantilever. This decrease in resonance frequency combined with the feedback loop system maintains a constant oscillation amplitude or frequency by adjusting the average tip-to-sample distance. Measuring the tip-to-sample distance at each (x, y) data point allows the scanning software to construct a topographic image of the sample surface.

Non-contact mode AFM does not suffer from tip or sample degradation effects that are sometimes observed after taking numerous scans with contact AFM. This makes non-contact AFM preferable to contact AFM for measuring soft samples. In the case of rigid samples, contact and non-contact images may look the same. However, if a few monolayer of adsorbed fluid are lying on the surface of a rigid sample, the images may look quite different. An AFM operating in contact mode will penetrate the liquid layer to image the underlying surface, whereas in non-contact mode an AFM will oscillate above the adsorbed fluid layer to image both the liquid and surface.

Schemes for dynamic mode operation include frequency modulation and the more common amplitude modulation. In frequency modulation, changes in the oscillation frequency provide information about tip-sample interactions. Frequency

can be measured with very high sensitivity and thus the frequency modulation mode allows for the use of very stiff cantilevers. Stiff cantilevers provide stability very close to the surface and, as a result, this technique was the first AFM technique to provide true atomic resolution in ultra-high vacuum conditions [91].

In amplitude modulation, changes in the oscillation amplitude or phase provide the feedback signal for imaging. In amplitude modulation, changes in the phase of oscillation can be used to discriminate between different types of materials on the surface. Amplitude modulation can be operated either in the non-contact or in the intermittent contact regime. In dynamic contact mode, the cantilever is oscillated such that the separation distance between the cantilever tip and the sample surface is modulated.

Amplitude modulation has also been used in the non-contact regime to image with atomic resolution by using very stiff cantilevers and small amplitudes in an ultra-high vacuum environment.

Tapping mode

Single polymer chains (0.4 nm thick) recorded in a tapping mode under aqueous media with different pH [92].

In ambient conditions, most samples develop a liquid meniscus layer. Because of this, keeping the probe tip close enough to the sample for short-range forces to become detectable while preventing the tip from sticking to the surface presents a major problem for non-contact dynamic mode in ambient conditions. Dynamic contact mode (also called intermittent contact or tapping mode) was developed to bypass this problem [93].

In tapping mode, the cantilever is driven to oscillate up and down at near its resonance frequency by a small piezoelectric element mounted in the AFM tip holder

similar to non-contact mode. However, the amplitude of this oscillation is greater than 10 nm, typically 100 to 200 nm. Due to the interaction of forces acting on the cantilever when the tip comes close to the surface, Van der Waals force, dipole-dipole interaction, electrostatic forces, etc. cause the amplitude of this oscillation to decrease as the tip gets closer to the sample. An electronic servo uses the piezoelectric actuator to control the height of the cantilever above the sample. The servo adjusts the height to maintain a set cantilever oscillation amplitude as the cantilever is scanned over the sample. A tapping AFM image is therefore produced by imaging the force of the intermittent contacts of the tip with the sample surface.

This method of "tapping" lessens the damage done to the surface and the tip compared to the amount done in contact mode. Tapping mode is gentle enough even for the visualization of supported lipid bilayers or adsorbed single polymer molecules (for instance, 0.4 nm thick chains of synthetic polyelectrolytes) under liquid medium. With proper scanning parameters, the conformation of single molecules can remain unchanged for hours [92].

1.4.7.3 AFM cantilever deflection measurement

Laser light from a solid state diode is reflected off the back of the cantilever and collected by a position sensitive detector (PSD) consisting of two closely spaced photodiodes whose output signal is collected by a differential amplifier. Angular displacement of cantilever results in one photodiode collecting more light than the other photodiode, producing an output signal (the difference between the photodiode signals normalized by their sum) which is proportional to the deflection of the cantilever. It detects cantilever deflections <10 nm (thermal noise limited). A long beam path (several centimeters) amplifies changes in beam angle.

REFERENCES

1.   Kashani H., Structural, Electrical and optical properties of zinc oxide produced by oxidation of zinc thin films, *J. Electron. Mater.,* 1998, **27**, 876−882.

2.   Wang M., Wang X., P3HT/ZnO bulk-heterojunction solar cell sensitized by a perylene derivative, *Sol. Energ. Mat. Sol. C.*, 2008, **92**, 766−771.

3.   Hongsith N., Viriyaworasakul C. Mangkorntong P., Mangkorntong N., Choopun S., Ethanol sensor based on ZnO and Au-doped ZnO nanowires, *Ceram. Int*., 2008, **34**, 823−826.

4.   Kingand D. S., Nix R. M., Thermal stability and reducibility of ZnO and Cu/ZnO catalysts, *J. Catal.,* 1996, **160**, 76−83.

5.   Boily S., Alamdari H.D., Cross G., Jolly A., VanNeste A., Grutter P., Schulz R., Ball milled ZnO for varistor application, synthesis and properties of mechanically alloyed and nanocrystalline materials, *Mater. Sci. Forum,* 1997, **235**, 993−998.

6.   Rensmo H., Keis K., Lindstrom H., Sodergren S., Solbrand A., Hagfeldt A., Lindquist S.E., Wang L.N., Muhammed M., *J. Phys. Chem*. B, 1997, **101**, 2598−2601.

7.   Pratsinis S.E., Flame aerosol synthesis of ceramic powders, *Prog. Energ Combust.,* 1998, **24**, 197−219.

8.   Strobel R., Krumeich F., Stark W.J., Pratsinis S.E., Baiker A., Flame spray synthesis of Pd/Al$_2$O$_3$ catalysts and their behavior in enantioselective hydrogenation. *J. Catal*., 2004, **222**, 307−314.

9.   Özgür Ü., Alivov Y. I., Liu C., Teke A., Reshchikov M. A., Doğan S., Avrutin V., Cho S.-J., Morkoç H., A comprehensive review of ZnO materials and devices. *J. Appl. Phys.,* 2005*,* **98**, 041301(1) −041301(103).

10. Wang Z.L., Kong X.Y., Zuo J.M., Induced growth of asymmetric nanocantilever a rrays on polar surfaces, *Phys. Rev. Lett.,* 2003, **91**, 185502.

11. Wang Z. L., Zinc oxide nanostructures: growth, properties and applications, *J. Phys-Condens. Mat.,* 2004, **16**, R829−R858.

12. Wang Z. L., Kong X. Y., Ding Y., P. Gao X., Hughes W. L., Yang R. S., Zhang Y., Semiconducting and Piezoelectric Oxide Nanostructures Induced by Polar Surfaces, *Adv. Funct. Mater.,* 2004, **14**, 943−956.

13. Hernandezbattez A., Gonzalez R., Viesca J., Fernandez J., Diazfernandez J., MacHado A., Chou R., Riba J., CuO, ZrO_2 and ZnO nanoparticles as antiwear additive in oil lubricants. *Wear*., 2008, **265**, 422−428.

14. Porter F., *Zinc Handbook: Properties, Processing, and Use in Design*. CRC Press. 1991.

15. Andrea D.C., Michel P, Raffaele R., Alfonso B., Ab initio study of piezoelectricity and spontaneous polarization in ZnO. *Phys. Rev. B:* 1994, **50**, 10715−10721.

16. Özgür Ü., Alivov, Y.I., Liu C., Teke A., Reshchikov M.A., Doğan S., Avrutin V., Cho S.-J., A comprehensive review of ZnO materials and devices. *J. Appl. Phys.,* 2005, **98**, 041103−041301.

17. Look D.C., Hemsky J.W., Sizelove J.R., Residual Native Shallow Donor in ZnO. *Phys. Rev. Lett.,* 1999, **82**, 2552−2555.

18. Janotti A., Van De Walle C.G., Van De Walle C.G., Hydrogen multicentre bonds. *Nat. Mater.,* 2007, **6** 44−47.

19. Kato H., Growth and characterization of Ga-doped ZnO layers on a-plane sapphire substrates grown by molecular beam epitaxy, *J. Cryst. Growth,* 2002, **237−239**, 538−543.

20. Takeshi O., Naoki O., Shigeaki S., Haruki R., Isao S., Yutaka A., Hajime H., Positive Hall coefficients obtained from contact misplacement on evident *n*-type ZnO films and crystals, *J. Mater. Res.,* 2008, **23**, 2293−2295.

21. Özgür Ü., Alivov, Ya I., Liu C., Teke A., Reshchikov M.A., Doğan S., Avrutin, V., Cho S.-J., A comprehensive review of ZnO materials and devices. *J. Appl. Phys.,* 2005, **98**, 041103−041301.

22. Wagner P., Helbig R., Halleffekt und anisotropie der beweglichkeit der elektronen in ZnO. *J. Phys. Chem. Solids,* 1974, **35**, 317−335.

23. Norton D.P., Heo Y.W., Ivill M.P., Ip H., Pearton S.J., Chisholm M.F., Steiner T., ZnO: growth doping & processing, *Mater. Today,* 2004, **2**, 34−40.

24. Kashani H., Structural, Electrical and optical properties of zinc oxide produced by oxidation of zinc thin films, *J. Electron. Mater*., 1998, **27**, 876−882.

25. Dayan N.J., Sainkar S.R., Karekar R.N., Aiyer R.C., Formulation and characterization of ZnO:Sb thick-film gas sensors, *Thin Solid Films,* 1998, **325**, 254−258.

26. Poulios I., Tsachpinis I., Photodegradation of the textile dye, *J. Chem. Technol. Biot*., 1999, **74**, 349−357.

27. Jung K.Y., Kang Y.C., Park S.B., Photodegradation of trichloroethylene using nanometre-sized ZnO particles prepared by spray pyrolysis, *J. Mater. Sci. Lett.,* 1997, **16**, 1848–1849.

28. Iwasaki J., Satoh M., Masuda T., Fujita T., Fabrication of Multi-Filamentary Y123 Superconductor, *J. Mater. Sci.,* 2000, **35,** 1603–1606.

29. Femg Y.J., Ming L.Y., Wei L.H., Chun L.Y., Hui L.B, Wu F.X., Growth and properties of ZnO nanotubes grown on Si(1 1 1) substrate by plasma-assisted molecular beam epitaxy. *J. Cryst. Growth,* 2005, **280**, 206–211.

30. Han D., Ren X.L., Chen D., Tang F.Q., Wang D., Ren J., Preparation and photocatalytic property of ZnO nanoparticles. *J. Photogra. Sci. Photochem.,* 2005, **23**, 414–415.

31. Rajalakshmia M., Arora A.K., Bender B.S., Mahamuni S., Optical phonon confinement in zinc oxide nanoparticles. *J. Appl. Phys.*, 2000, **87**, 2445–2446.

32. Oh B.Y., Jeong M.C., Moon T.H., Lee W., Myoung J.M., Hwang J.Y., Seo D.S., Transparent conductive Al-doped ZnO films for liquid crystal displays. *J. Appl. Phys.,* 2006, **99**, 124505–124506.

33. Nomura K., Ohta H., Ueda K., Kamiya T., Hirano M., Hosono H., Thin-Film Transistor Fabricated in Single-Crystalline Transparent Oxide Semiconductor. *Science*, 2003, **300,** 1269-1272.

34. Heo Y.W., Tien L.C., Kwon Y., Norton D.P., Pearton S.J., Kang B.S., Ren F., Depletion-mode ZnO nanowire field-effect transistor. *Appl. Phys. Lett.,* 2004, **85**, 2274–2276.

35. Ohtomo A., Tamura K., Kawasaki M., Makino T., Segawa Y., Tang Z.K., Wong G.K.L., Matsumoto Y., Koinuma H., Roomtemperature stimulated emission of excitons in ZnO/(Mg, Zn)O superlattices. *Appl. Phys. Lett.,* 2000, **77**, 2204–2206.

36. Assuncao V., Fortunato E., Marques A., Ağuas H., Ferreira I., Costa M.E.V., Martins R., Influence of the deposition pressure on the properties of transparent and conductive ZnO:Ga thin-film produced by r.f. sputtering at room temperature, *Thin Solid Films*, 2003, **427**, 401–405.

37. Bai S.N., Tsai H.H., Tseng T.Y., Structural and optical properties of Al-doped ZnO nanowires synthesized by hydrothermal method, *Thin Solid Films*, 2007, **516**, 155–158.

38. Miao L., Ieda Y., Tanemura S., Cao Y.G., Tanemura M., Hayashi Y., Toh S., Kaneko K., Synthesis, microstructure and photoluminescence of well-aligned ZnO nanorods on Si substrate, *Sci. Technol. Adv. Mater.*, 2007, **8**, 443–447.

39. Damontea L.C., Mendoza Ze0lisa L.A, Soucase B.M., Nanoparticles of ZnO obtained by mechanical milling. *Powder Technol.*, 2004, **148**, 15–19.

40. Kammler H.K., Mädler L., Pratsinis S.E., Flame synthesis of nanoparticles. *Chem. Eng. Technol.*, 2001, **24**, 583–596.

41. Peiniger M., Piel H., A Superconducting Nb_3Sn Coated Multicell Accelerating Cavity. *Nucl. Sci.,* 1985, **32**, 3610–3612.

42. Salles Mou H.R., Louremjo de Moura L., Melting And Purification Of Niobium, *AIP Conference Proceedings* (American Institute of Physics)

(927(Single Crystal - Large Grain Niobium Technology)), 2007, 165–178.

43. N. Izabela., Z Maria., Niobium Compounds: Preparation, Characterization, and Application in Heterogeneous Catalysis, *Chem. Rev., 1999,* **99**, 3603–3624

44. Jahnke L.P., Frank R.G., Redden T.K., Columbium Alloys Today. *Metal Progr.,* 1960, **77**, 69–74.

45. Nikulina A.V., Zirconium-Niobium Alloys for Core Elements of Pressurized Water Reactors. *Met. Sci. Heat Treat.,* 2003 **45**, 287–292.

46. http://environmentalchemistry.com/yogi/periodic/Au.html

47. Lide D.R., *CRC Handbook of Chemistry and Physics*, CRC Press, Boca Raton, 2004.

48. Gupta C. K., Suri A. K., *Extractive Metallurgy of Niobium*, CRC Press, Boca Raton, 1994.

49. Holleman A.F., Wiberg E., Wiberg N., Niob (in German). *Lehrbuch der Anorganischen Chemie*, Walter-de-Gruyter-Verlag, Berlin, New York, 1985.

50. Greenwood N.N., Earnshaw A., *Chemistry of the Elements*, Oxford: Butterworth-Heinemann, Oxford, 1997.

51. http://www.lenntech.com/periodic/elements/nb.htm (December, 12 2010)

52. Lin J.M., Zhang Y.Z., Ye, Z.Z., Gu X.Q., Pan X.H., Yang Y.F., Lu J.G., He H.P., and Zhao B. H., Nb-doped ZnO transparent conducting films fabricated by pulsed laser deposition. *Appl. Surf. Sci.* 2009, **255**, 6460–6463.

53. Kudo M., Kosaka T., Takahashi Y., Kokusen H., Sotani N., Hasegawa S., Sensing Functions to NO and O_2 of Nb_2O_5 - or Ta_2O_5 -Loaded TiO_2 and ZnO, *Sens. Actuators B: Chem.*, 2000. **69**, 10−15.

54. Teleki A.**,** Bjelobrk N., Pratsiniset S. E., Flame-made Nb- and Cu-doped TiO_2 sensors for CO and ethanol, *Sens. Actuators B: Chem.*, 2008, 130, 449−457.

55. Siddiki M.K., Munoz-Rojas D., Oro J., Jing J. u, Qia Q., Galipeau D. W. and ura-cantu M., Synthesis and Characterization of Nb doped Titania for Dye Sensitized Solar Cells, *IEEE* Photovoltaic Specialists Conference, 2009, 685−689.

56. Hinklin T., Toury B., Gervais C., Babonneau F., Gislason J.J., Morton R.W., Laine R.M., Liquid-feed flame spray pyrolysis of metalloorganic and inorganic alumina sources in the production of nanoalumina powders. *Chem. Mater.,* 2004, *16*, 21−30.

57. Limaye A.U., Helble J.J., Morphological control of zirconia nanoparticles through combustion aerosol synthesis. *J. Am. Ceram. Soc.,* 2002, *85*, 1127−1132.

58. Mädler L., Stark W.J., Pratsinis S.E., Rapid synthesis of stable ZnO quantum dots. *J. Appl. Phys.,* 2002, *92*, 6537−6540.

59. Strobel R., Stark W.J., Mädler L., Pratsinis S.E., Baiker A., Flame-made platinum/alumina: structural properties and catalytic behaviour in enantioselective hydrogenation. *J. Catal.,* 2003, *213*, 296−304.

60. Keskinen H., Makela J., M., Vippola M., Nurminen M., Liimatainen J., Lepisto T., Keskinen J., Generation of silver/ palladium nanoparticles by liquid flame spray. *J. Mater. Res.,* 2004, *19*, 1544–1550.

61. Mueller R., Mädler L., Pratsinis S.E., Nanoparticle synthesis at high production rates by flame spray pyrolysis. *Chem. Eng. Sci.,* 2003, *58*, 1969–1976.

62. Mädler L., Pratsinis S.E., Bismuth oxide nanoparticles by flame spray pyrolysis. *J. Am. Ceram. Soc.,* 2002, *85*, 1713–1718.

63. Mueller R., Jossen R., Kammler H. K., Pratsinis S. E., Akhtar M. K., Growth of zirconia particles made by flame spray pyrolysis. *AIChE J.,* 2004, *50*, 3085–3094.

64. Tani K., Mädler L., Pratsinis S.E., Homogeneous ZnO nanoparticles by flame spray pyrolysis. *J. Nanopart. Res.*, 2002, **4,** 337–343

65. Karthikeyan J., Berndt C. C., Tikkanen J., Wang J. Y., King A. H., Herman H., Nano material powders and deposits prepared by flame spray processing of liquid precursors, *Nanostruct. Mater.,* 1997, **8**, 61–74.

66. Sokolowski M., Sokolowska A., Michalski A. and Ziolkowski Z., Synthesis of Al_2O_3 from the vapour in an extermal electric field, *J. Cryst. Growth*, 1981, **52**, 274–278.

67. Jang Y. J., Simer C., Ohm T., Comparison of zinc oxide nanoparticles and its nanocrystalline particles on the photocatalytic degradation of methylene blue, *Mater. Res. Bull.*, 2006, **41**, 67–77.

68. Kodas T., Hampden-Smith M.J., *Aerosol Processing of Materials*, Wiley-VCH, New York, 1999.

69. Messing G. L., Zhang S. C., Jayanthi G. V., Synthesis of ceramic powder by flame spray pyrolysis, *J. Am. Ceram. Soc.,* 1993, **76**, 2707–2726.

70. Hinds W. C., *Aerosol Technology: Properties, Behavior, and Measurement of Airborne Particles.* A John Wiley & Sons, New York, 1982.

71. http://nobelprize.org/nobel_prizes/physics/laureates/1921/press.html. (December, 12 2010)

72. Raman V., Fox R.O., Gordon M., *Development of a Predictive Multiphysics Computational Model for Nanoparticle Synthesis Using Flame-Spray Pyrolysis*, NSF Research Proposal, 2007.

73. Cullity B.D., *Elements of X-ray Diffraction*, Massachusetts: Addison-Wesley, Reading, Washington D.C., 1978.

74. Cruz A.B., Shen Q., Toyoda T., The Effect of Ultraviolet Irradiation on the Photothermal, Photoluminescence and Photoluminescence Excitation Spectra of Mn-Doped ZnS Nanoparticles, *Thin Solid Films*, 2006, **499,** 104–109.

75. Li G.H., Su F.H., Ma B.S., Ding K., Xu S.J., Chen W., Photoluminescence of doped ZnS nanoparticles under hydrostatic pressure, *Phys. Status Solidi B*, 2004, **241**, 3248–3256.

76. Brunauer S., Emmett P., Teller P.H., Adsorption of gases in multimolecular layers. *J. Am. Chem. Soc.,* 1938, **60**, 309–319.

77. Goldstein J., *Scanning Electron Microscopy and x-ray Microanalysis.* Kluwer Adacemic/Plenum Pulbishers, New York, 2003.

78. Tanaka M., Qi J., Masumoto Y., Comparison of energy levels of Mn^{2+} in nanosized- and bulk-ZnS crystals, *J. Lumin.,* 2000, **87–89**, 472–474.

79. http://www.microscopy.ethz.ch/sem.htm (December, 12 2010)

80. Tanabe Y., Sugano S., On the absorption spectra of complex ions, *J. Phys. Soc. Jpn.,* 1954, **9**, 753−779.

81. Severin K.P., *Energy Dispersive Spectrometry of Common Rock Forming Minerals,* Kluwer Academic Publishers, New York, 2004, 225.

82. Goldstein J., *Scanning Electron Microscopy and X-ray Microanalysis*. Kluwer Adacemic/Plenum Pulbishers, New York, 2003.

83. Tanabe Y., Sugano S., Absorption spectra of Cr^{3+} in $Al_2O_3(A)$. Theoretical studies of the absorption bands and lines, *J. Phys. Soc. Jpn.,* 1954, **9**, 753−767.

84. Bhattacharjee B., Ganguli D., Iakoubovskii K., Stesmans A., Chaudhuri S., Synthesis and characterization of sol–gel derived $ZnS:Mn^{2+}$ nanocrystallites embedded in a silica matrix Bull. *Mater. Sci.,* 2002, **25**, 175−180.

85. http://www.hk-phy.org/atomic_world/tem/tem02_e.html. (December, 12 2010)

86. Skoog D.A., West D.M., Holler F.J., Crouch S.R., *Fundamentals of Analytical Chemistry 8th ed.,* Brooks/Cole – Thomson Learning, Redwood City, 2004.

87. Shionoya S. and Yen W.M., *Phosphor Handbook,* CRC Press, Boca Raton, 1999.

88. Sykes A.G., *Advances in inorganic chemistry*, Academic Press., San Diego, 1999.

89.   Powell R.C., *Physics of Solid-State Laser Materials,* Springer-Verlag, New York, 1998.

90.   http://comp.uark.edu/~jchakhal/AFM%20scans.htm. (December, 12 2010)

91.   Giessibl F.J., Advances in atomic force microscopy. *Rev. Mod. Phys*, 2003, **5**, 949.

92.   Roiter Y., Minko S., AFM single molecule experiments at the solid-liquid interface: in situ conformation of adsorbed flexible polyelectrolyte chains. *J. Am. Chem. Soc.,* 2005, **127**, 15688‒15689.

93.   Zhong Q., Inniss D., Kjoller K., Elings V., Fractured polymer/silica fiber surface studied by tapping mode atomic force microscopy. *Surf. Sci. Lett.,* 1993, **290,** 688‒692.